CIT. Journal of Computing and Information Technology, Vol. 31, No. 3, September 2023, 137–150
doi: 10.20532/cit.2023.1005746


# Signal Processing and Channel Modelling for 5G Millimeter-Wave Communication Environment

Yu Qian

School of Rail Transportation, Southwest Jiaotong University Hope College, Chengdu, Sichuan, China

Compared to frequency bands below 6 GHz, 5G millimeter waves offer several advantages, including a large bandwidth, minimal null delay, and flexible null port configuration. To comprehend the channel characteristics of 5G millimeter-wave technology, conducting channel measurements on it is essential. Hence, to ensure precise 5G millimeter-wave channel measurements and facilitate channel modelling, this study recommends utilizing a phased array antenna-based method for channel measurement. The experimental outcomes demonstrated that the shadow fading term of the actual measurement data follows a normal distribution in both line-of-sight and non-line-of-sight scenarios. Additionally, the K-S test confirms that all Boolean variables are equal to 1 and all numerical variables are greater than α. The line-of-sight scenario produces a logarithmic mean delay extension of –7.4 and a standard deviation of 0.12, based on actual measured data. Meanwhile, 3GPP shows a logarithmic mean of –7.4 and a standard deviation of 0.15. In the non-line-of-sight scenario, the logarithmic mean delay extension is –7.3 with a standard deviation of 0.17, while 3GPP produces a logarithmic mean of –7.4 and a standard deviation of 0.19. The data presented closely adheres to the 3GPP model. It is evident that the channel measurement method, proposed within the study, effectively measures the parameters within the delay domain. Concerning the prolonged pitch angle and azimuth angle ranges, they measure 14°–31° and 14°–29° in the line-of-sight situation, and 21°–33° and 19°–37° in the corresponding non-line-of-sight situation. Additionally, the logarithmic mean and standard deviation for both the pitch angle and azimuth angle in the line-of-sight scenario are 1.32 and 0.09, respectively. The logarithmic mean and standard deviation of the azimuth angle of arrival are 1.35 and 0.08, respectively. The above results show that the method proposed in the study enables the measurement of 5G millimeter-wave channels and is important for millimeter-wave channel modelling.

*ACM CCS (2012) Classification:* Hardware → Communication hardware, interfaces and storage → Sensor devices and platforms
Networks → Network types → Mobile networks

*Keywords*: 5G, millimeter wave, channel measurement, phased array antenna, measurement waveform, waveform analysis

## 1. Introduction

5G technology is advantageous for digital development due to its low latency, high speed, low power consumption, and ability to connect everything. However, the increased peak rate of 5G as compared to 4G creates greater demands on spectrum bandwidth. The bandwidth of millimeter waves (MW) can reach as high as 273.5 GHz, while the total bandwidth for propagation in the atmosphere through the four primary windows is 135 GHz [1–2]. Whilst MW bandwidth resources are indeed abundant and can offer significant support for the progression and utilization of 5G, it is important to note that 5G millimeter-wave technology (5G-MW) is not without its flaws. Specifically, 5G-MW is known to exhibit greater loss and attenuation in comparison to band 4, attributable to its heightened susceptibility to environmental influences such as precipitation [3-4]. Therefore, to ensure effective use of 5G-MW, a thorough understanding of its channel transmission characteristics is necessary. The primary aim of channel measurement (CM) is to extract channel pa-

rameters. Once the transmitter sends the measurement signal, it passes through the measured channel to reach the receiver. By analyzing the path parameters of the received signal and other relevant information, it is possible to obtain channel statistical parameters. It is important to explain any technical term abbreviations when they are first used. The present widely utilized CM tool is the vector network analyzer. However, its transmitter and receiver are integrated, leading to significant feedline loss. Additionally, the slow scanning speed of this device limits its suitability to short-range CMs, and it cannot accurately measure channels that are time-varying. In microwave CMs, the precision of angle data is dependent on the number of physical antennas. The higher the quantity of antennas, the more precise the resolution. However, it is challenging to move the physical antenna, rendering it suitable only for static scenes. During CM, omnidirectional or low gain antennas are used to transmit and receive radio wave signals from all spatial angles. However, high gain directional antennas are necessary to ensure adequate signal strength, and these can only receive signals at a specific angle. This requires splicing multiple directional antennas in different directions or employing virtual array rotation. The measurement of millimeter-wave channels presents challenges due to their large bandwidth characteristics. High system synchronization and calibration accuracy are required, as well as fast data storage speed and complex parameter analysis. Consequently, to compensate for the limitations of current CM devices and attain MWCM for dynamic scenarios, this study proposes a phased-array antenna (PAA)-based CM method to achieve accurate measurements of the MW channel and provide strong support for channel modelling, network deployment planning, *etc.* This method employs phased array to achieve swift measurement of angle information across the entire space by rapidly scanning the beam. This caters to the requirements of dynamic measurement both indoors and outdoors while ensuring antenna gain and retaining a vast measurement dynamic range. Additionally, the study conducted CMs of the 5G millimeter-wave scene and obtained corresponding analysis results. These research findings will greatly advance the development of CM in the 5G millimeter-wave frequency band, supporting millimeter-wave channel modeling, wireless communication system design, network deployment planning, and equipment performance testing.

The article comprises four sections. The initial section discusses the research on 5G-MW and PAA. The second section examines in depth the 5G-MWCM approach based on PAA. The third part assesses the CM outcomes, and the last section provides a summary of the whole study.

With the rapid development of 5G technology, research related to 5G-MW channels is receiving increasing attention. An enlarged annular lens antenna with high gain has been proposed by Z. Zhang *et al.* for 5G-MWCM [5]. An enlarged circular lens and an omnidirectional feed were features of the antenna, the latter of which effectively increases the vertical radiation aperture and boosts the omnidirectional gain. Jericho *et al.* have shown that a stable vertically polarized omnidirectional radiation pattern in the target band, with a –10 dB impedance bandwidth of 20.7% for the antenna [6]. T. Jiang *et al.* proposed a multipath extraction algorithm based on the spatial alternating generalized expectation maximization algorithm for the spatial feature distribution of uplink and downlink channels in 28 GHz urban micro-scenarios and clustered MPCs by the spatial flap method [7]. The experimental results revealed that the azimuthal arrival angles showed Gaussian distribution in the uplink and downlink channels. H. Mi *et al.* proposed a vector network analyzer based MWCM instrument for the study of wireless channel sparsity and used the root mean square delay expansion, Gini index and Rician K factor for the measurement of channel sparsity [8]. The experimental results showed that the antenna steering and scattering environment had a large impact on channel sparsity. A ray tracing-based PL prediction technique was proposed by Q. Zhu *et al.* to investigate UAV MW channel loss [9]. The algorithm's ability to predict PL values at various altitudes with a guaranteed modest standard deviation was demonstrated by the experimental findings. S. H. Lim *et al.* proposed a deep learning-based beam tracking method for the problem of how one can achieve MW beam tracking [10]. Cho *et al.* used deep neural network analysis of the inertial sensor signal to analyze the time structure of the time-varying channel and predict its distribution with LSTM. The experimental

results demonstrated that the method had significant performance gain compared to the traditional method [11].

Because of its high beam scanning speed and quick phase shift, PAA is an antenna that modifies the form of the directional map by adjusting the feed phase of the radiating units in the array antenna. It is widely utilized in a variety of fields. R. Xiao *et al.* have proposed a sparse PAA with a sparsity of 4% to address the problem of how to improve the performance of W-band radar [12]. The antenna adopts waveguide feed as the antenna unit, which reduces the feed loss and improves the antenna gain. The experimental results showed that the normal and scanning sidelobe levels were lower than –18 dB and –13 dB, respectively. T. Hirasawa *et al.* proposed an integrated photonic array antenna system based on RoF for the problem of quantitative RF power variations in next-generation MW-band wireless networks, which consists of a 4 × 2 array of 60 GHz patch antennas and high-speed photodiodes [13]. The system was tested for its high RF transmission efficiency and its ability to form a remote antenna beam. Z. Zhou *et al.* have addressed the issue of how to obtain quick and high-precision offline estimation of the beam formation direction map of active PAA by proposing a modelling approach that incorporates all component states [14]. According to the experimental results, Cho and Chun's research can efficiently obtain the relevant beam control code for an active phased array antenna (PAA), which significantly reduces the effort required for beam measurement and online compensation [15]. E. S. Parshina addressed the problem of how to improve the performance of a single pulse radar by proposing a PAA with a low paraflap aperture distribution. The antenna was tested to meet the requirements of a paraflap fading system with only one subgraph [16]. Li *et al.* proposed a data transmission technique utilizing PAA to mitigate the challenge of real-time marine seismic data transmission [17]. Test findings indicated that the transmission distance of PAA can reach 105 km, the transmission delay was not more than 3 s, and the transmission rate and loss were 40 Kbps and 1.5%, respectively. It could be seen that PAA can achieve real-time transmission of seismic data in the marine area.

In summary, research on various aspects of MW channels has been quite fruitful, but all these research works need MWCM to provide support for them. Therefore, to achieve precise measurements of MW channels, this study proposes a 5G-MWCM method that utilizes PAA, which provides robust support for modeling MW channels, designing wireless communication systems, and other related applications.

## 2. Research Method

With the development of wireless communication technology, 5G technology has begun to gradually penetrate people's lives. 5G-MW has abundant bandwidth resources, which greatly improves the communication rate. But at the same time, due to the characteristics of MW, it also brings challenges to channel modelling. Therefore, in order to provide strong support for channel modelling of 5G-MW, the study proposes a PAA-based MWCM system.

### 2.1. 5G-MWCM Waveform Generation and Parsing Methods

The measurement outcomes in CM are significantly impacted by the measuring signal selection. The accuracy of CM requires a measurement signal with a wide bandwidth, duration meeting channel parameters, power spectral density at constant amplitude frequency points, small peak-to-average power ratio, and strong correlation. Therefore, after fully considering the above requirements, the study chooses a measurement waveform generation method based on the Zadoff-Chu sequence. The Zadoff-Chu sequence is shown in equation (1).

$$x_u(n)=\begin{cases} e^{-j\pi\frac{un(n+1)}{N_{ZC}}} \cdots N_{ZC}=\text{Odd number} \\ e^{-j\pi\frac{un^2}{N_{ZC}}} \cdots N_{ZC}=\text{Even number} \end{cases} \quad (1)$$

In equation (1), $x_u(n)$ denotes the Zadoff-Chu sequence, $N_{ZC}$ is the length of the sequence, $n$ is the index of the element in the sequence, and $u$ is the root index of the sequence. After generating the Zadoff-Chu sequence, the complex transform is performed on it. Then the frequency domain signal is achieved after the parame-

ters of bandwidth and sampling rate sampling point are configured [18]. Finally, the baseband signal can be obtained by the inverse Fourier transform. The baseband signal expression is shown in equation (2).

$$s_{base} = s_{real} + i \cdot s_{imag} \tag{2}$$

In equation (2), $s_{base}$ denotes the baseband signal, $s_{real}$ denotes the real part of the signal, and $s_{imag}$ denotes the imaginary part of the signal. Because the frequency centers of the created baseband signal are only 1.6 GHz, while the frequency centers of the IF inputs and outputs at the transmitter and receiver are 1.8 GHz, digital up-conversion is necessary once the measurement signal is formed [19]. The digital up-conversion calculation is shown in equation (3).

$$\begin{aligned} s_{up} &= s_{real} \cdot \sin\left(\frac{\Delta f \cdot 2\pi \cdot i}{Fs}\right) \\ &+ s_{imag} \cdot \sin\left(\frac{\pi}{2} + \frac{\Delta f \cdot 2\pi \cdot i}{Fs}\right) \ldots \\ i &= 0, 1, \ldots, N-1 \end{aligned} \tag{3}$$

In equation (3), $s_{up}$ denotes the signal after digital up-conversion, $\Delta f$ denotes the migration frequency with value of 200 MHz, $Fs$ denotes the sampling rate with value of 3.2 Gsample/s, and $N$ denotes the number of sampling points. The principle of the digital up-converter is shown in Figure 1.

In Figure 1, the main components of the digital up-converter are the interpolation filter and the numerically controlled oscillator (NCO). After the baseband signal is generated, it is divided into two parts and processed separately by the interpolation filter and then frequency shifted by the NCO [20, 21]. After digital up-conversion, the frequency center of the sampled signal becomes 1.8 GHz. However, when waveform resolution is performed, it needs to be digitally down-converted (DDC) as the signal comment is required to be at frequency 0. The digital down-conversion calculation equation is shown in equation (4).

$$\begin{aligned} r_{base} &= r_{down} \cdot \sin\left(\frac{\Delta f \cdot 2\pi \cdot i}{Fs}\right) \\ &+ r_{down} \cdot \sin\left(\frac{\pi}{2} + \frac{\Delta f \cdot 2\pi \cdot i}{Fs}\right) \ldots \\ i &= 0, 1, 2, \ldots, M-1 \end{aligned} \tag{4}$$

In equation (4), $r_{base}$ denotes the signal after digital down-conversion, $r_{down}$ denotes the signal after analogue-to-digital conversion (ADC) at the receiving end, the value of migration frequency $\Delta f$ is 1.8 GHz, the value of sampling rate $Fs$ is 6.4 Gsample/s, and $M$ denotes the number of points corresponding to the snap time at the receiving end [22]. The digital down-conversion structure is shown in Figure 2.

In Figure 2, the ADC sampled signal is divided into two ways, one way is multiplied with a sine wave and down-converted to frequency 0. The other way is multiplied with a cosine wave and down-converted to frequency 0; where both the sine and cosine waves are generated by the NCO. After the sampled signal is dig-

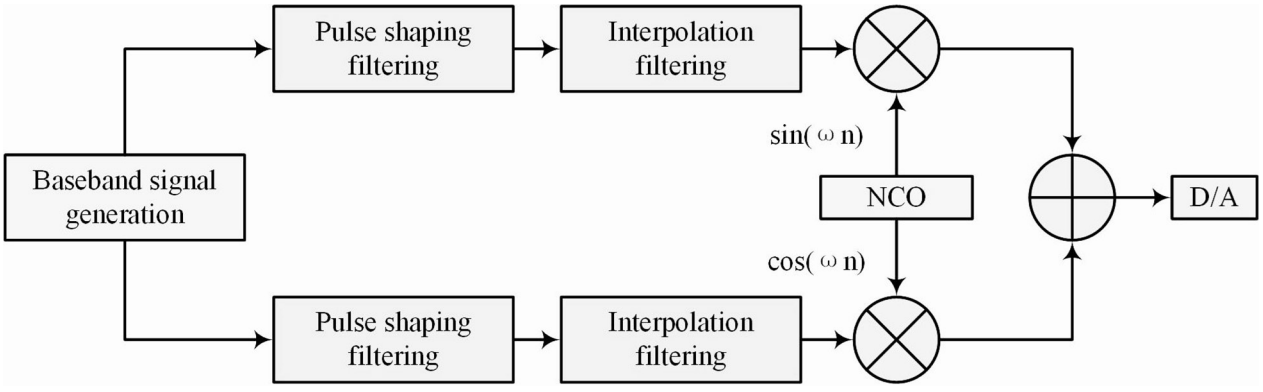


*Figure 1.* Principle of a digital up-converter.

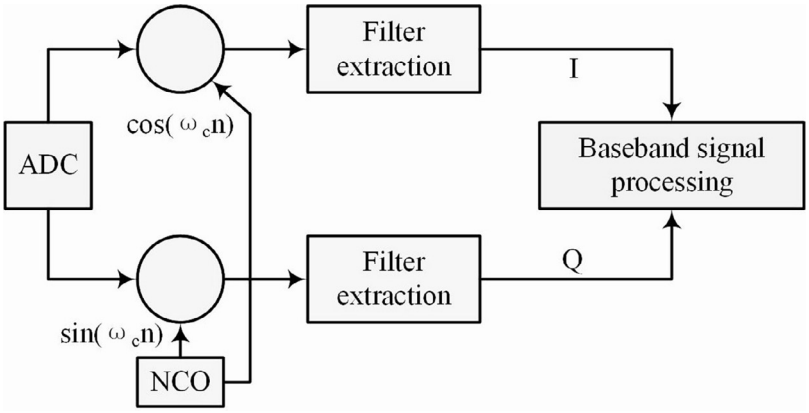


*Figure 2.* Digital down-conversion structure.

itally down-converted, the baseband complex data is obtained, and to facilitate its characterization, the impulse response matrix of the channel needs to be extracted [23–24]. The flow of channel impulse response acquisition is shown in Figure 3.

After converting a portion of data collected by the CM system into digital I (same direction) and Q (orthogonal) deconvolution data, it is necessary to extract the channel impulse response matrix and then analyze the channel characteristics. To get the channel impulse response matrix in Figure 3, three types of data are needed: the reference signal, the system calibration file, and the original measurement file. The system calibration file is obtained by directly measuring the transducer and receiver to eliminate the inherent response of the measurement system. It is crucial to obtain the system calibration file before each measurement, as the measurement system is susceptible to environmental interference. The received signal with the inherent response of the measurement system removed and the channel impulse response are calculated as shown in equation (5).

$$\begin{cases} F\left[r_{ch}\right] = \dfrac{F\left[r_{meas}\right]}{F\left[r_{sys}\right]} \\ r_{ch} = u * h \\ h = F^{-1}\left[\dfrac{F\left[r_{ch}\right]}{F\left[u\right]}\right] \end{cases} \tag{5}$$

In Equation (5), $r_{ch}$ denotes the received signal with the intrinsic response of the measurement system removed, $r_{meas}$ denotes the original measurement data, $r_{sys}$ denotes the system calibration data, $u$ denotes the reference signal, and $h$ denotes the channel impulse response.

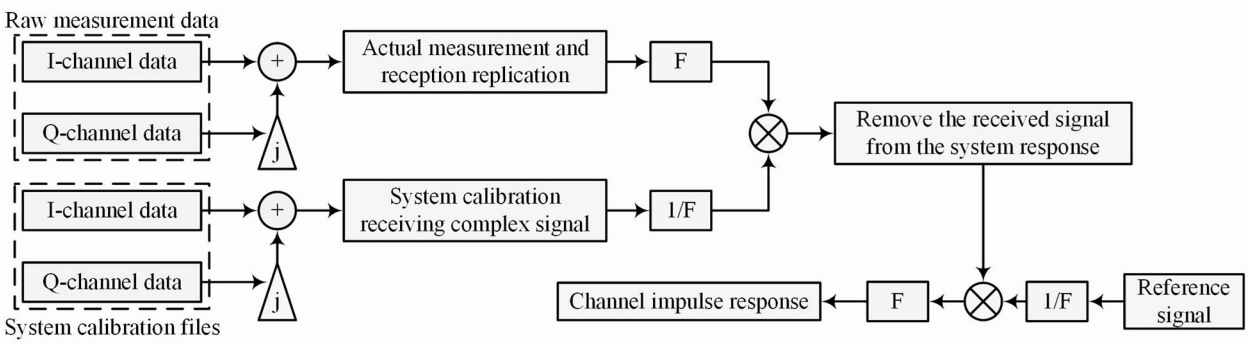


*Figure 3.* Acquisition process of the channel impulse response.

## 2.2. PAA-based MW Channel Parameter Extraction Method and System Design

When building the MW measurement system, the channel parameters of MW need to be extracted first. In the MWCM system, the PAA is used at the receiver side, which builds the virtual SIMO system by beam scanning. The CM signal model of the beam scanning virtual SIMO system is shown in Figure 4.

A transmission wall, a receiving wall, and a scatterer make up the entire model shown in Figure 4. The input signal arrives at the receiving wall from the transmitting wall through multiple paths. Then the signal calculation equation for each path is shown in equation (6).

$$\begin{cases} s(t,p_l)=\left[s_1(t,p_l),...,s_Q(t,p_l)\right]^T \\ \quad\quad =c(\theta_l,\phi_l)\alpha_l u(t-\tau_l) \\ p_l=[\tau_l,\theta_l,\phi_l,\alpha_l] \\ c(\theta,\phi)=\begin{bmatrix} c_1(\theta,\phi) \\ \cdots \\ c_Q(\theta,\phi) \end{bmatrix}=\begin{bmatrix} f(\theta-\overline{\theta}_1,\phi-\overline{\phi}_1) \\ \cdots \\ f(\theta-\overline{\theta}_Q,\phi-\overline{\phi}_Q) \end{bmatrix} \end{cases} \tag{6}$$

In equation (6), $s(t, p_l)$ denotes the signal of multipath $l$, $p_l$ denotes the parameter ensemble of multipath $l$, $t$ denotes the snap time, $\tau_l$ denotes the time delay of multipath $l$, $\theta_l$ denotes the vertical angle of arrival, $\phi_l$ denotes the horizontal angle of arrival, $\alpha_l$ denotes the amplitude, $c(\theta, \phi)$ denotes the guiding vector, and $Q$ denotes the number of scanning beams.

The matrix of the receiving antenna is shown in equation (7).

$$\begin{aligned} Y(t)&=\sum_{l=1}^{L}s(t,p_l)+\sqrt{\frac{N_0}{2}}N(t) \\ &=\left[Y_1(t),...,Y_D(t)\right]^T \end{aligned} \tag{7}$$

In equation (7), $Y(t)$ denotes the matrix of the receiving antenna, $L$ denotes the number of multipaths, $N(t)$ denotes the $D$-dimensional Gaussian white noise, and $N_0$ denotes a positive constant. The corresponding broadband received signal in the horizontal dimension is shown in equation (8).

$$y_i(\tau)=\sum_{l=1}^{L}\alpha_l \cdot f\left(\phi_l-\overline{\phi}_i\right)\cdot u(\tau-\tau_l) \tag{8}$$

In equation (8), $y_i(t, \tau)$ denotes the broadband received signal, $f$ denotes the antenna direction map with phase response and amplitude response, $u$ denotes the input signal, and $\overline{\phi}_i$ denotes the pointing of the $i$ beam. The channel impulse response of the $i$ beam and the synthetic channel impulse response are calculated in equation (9).

$$\begin{cases} h(i,\tau)=\sum_{l=1}^{L}\alpha_l \cdot f\left(\phi_l-\overline{\phi}_i\right)\cdot\delta(\tau-\tau_l) \\ h_{syn}(\tau)=\sum_i h(i,\tau)=\sum_{l=1}^{L}\alpha_l \cdot F_{syn}(\phi_l)\cdot\delta(\tau-\tau_l) \end{cases} \tag{9}$$

In equation (9), $h(i, \tau)$ denotes the channel impulse response, $\delta$ denotes the Dirac function, $h_{syn}(\tau)$ denotes the synthesized channel impulse response, and $F_{syn}(\phi_l)$ denotes the sum of the antenna directional maps with phase and

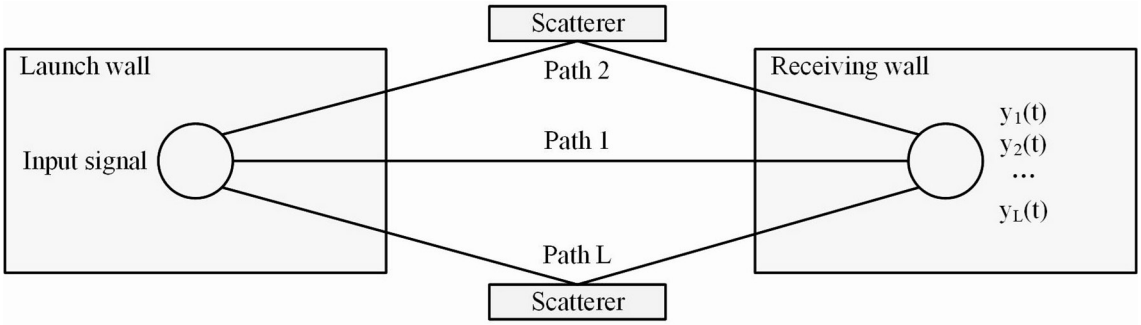


*Figure 4.* The channel measurement signal model of the beam-scan virtual SIMO system.

magnitude responses. Additionally, the power time delay spectrum represents the second-order moments of the synthetic channel impulse response. However, as the PAA is utilized at the receiver side, only the reach angle requires analysis. The power time-delay spectrum and power angle time-delay spectrum are calculated using equation (10).

$$\begin{cases} PDP_{sector} = \left|h_{syn}(\tau)\right|^2 = \left|\sum_{l=1}^{L} \alpha_l \bullet F_{syn}(\phi_l) \bullet \delta(\tau - \tau_l)\right|^2 \\ PADP(\theta_{RX}, \tau) = \left|F^{-1}\left\{W(\vec{f}) \cdot \frac{H_{\theta_{RX},\, omni_{TX}}(\vec{f})}{G_{\theta_{RX},\, omni_{TX}}(\vec{f})}\right\}\right|^2 \end{cases} \quad (10)$$

In equation (10), $PDP_{sector}$ denotes the power time-delay spectrum in the 90° sector area, *PADP* denotes the power angle time-delay spectrum, $\theta_{RX}$ denotes the phased array azimuth, $W(\vec{f})$ denotes the Hanning window, $\vec{f}$ denotes the frequency, $H_{\theta_{RX}, omni_{TX}}(\vec{f})$ denotes the calibrated frequency response, and $G_{\theta_{RX}, omni_{TX}}(\vec{f})$ denotes the joint antenna response at the transmitter. The multipath can be extracted from the power angle time delay spectrum, and the flow of the multipath extraction algorithm is shown in Figure 5.

In Figure 5, after initializing the list of multipaths, the peaks are searched and all peaks greater than the threshold are stored. Then, a time delay is selected and the multipath with the maximum power at that time delay is stored; finally, all the time delays are traversed and the corresponding multipaths are saved [25]. The MWCM system can be obtained by integrating all the above modules, and the system structure is shown in Figure 6.

In Figure 6, the system is divided into the transmitter and receiver side. After generating the baseband signal at the transmitter, it is initially digitally up-converted (DUC) to increase its frequency center. Then, it undergoes digital-to-analog conversion (DAC) and is processed by the up-conversion module. Overall, the signal is subjected to power amplification. The processed signal is transmitted to the receiving end via wireless signal transmission. The receiving end performs low-noise power amplification on the signal, processes it through the down-conversion module, and then performs ADC. Finally, all the data is stored and analyzed offline. To get the channel impulse response, the analogue-to-digital converted component of the data is DDC. In the system's CM, it is necessary to calibrate not only the mechanical energy of the system, but also test the power and path loss dynamic range [26]. For discrete signals, the signal power can be calculated by Parseval's theorem, which is given in equation (11).

$$\sum_{n=0}^{N-1}\left|x[n]\right|^2 = \frac{1}{N}\sum_{k=0}^{N-1}\left|X[k]\right|^2 \quad (11)$$

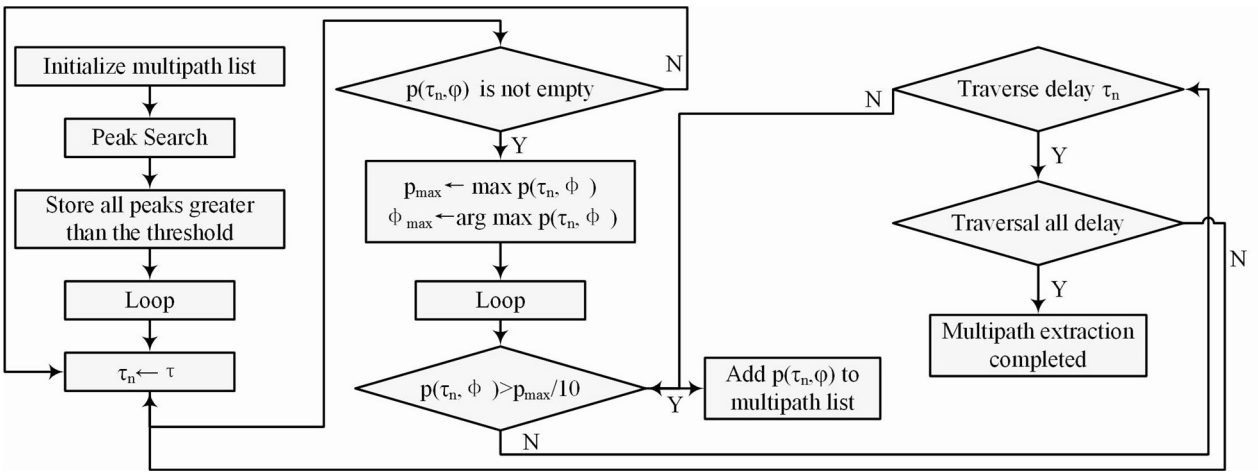


*Figure 5.* Flow of the multipath extraction algorithm.

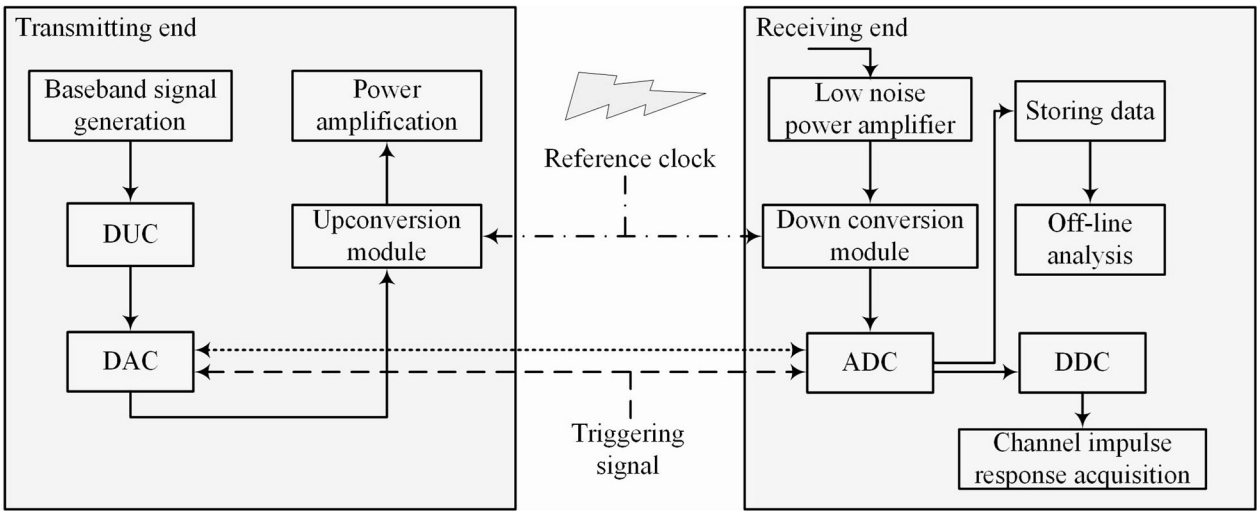


*Figure 6.* Structure of the mm-wave channel measurement system.

The time-domain signal is represented by $x[n]$ in equation (11), the equivalent frequency-domain signal is represented by $X[k]$, and the number of frequency points is represented by $N$ [25]. In the dynamic range test of path loss, only the absolute power difference between the transmitter and receiver is unable to accurately describe the path loss. This is because the difference in absolute power includes not only the path loss, but also the loss of RF screenshots and high-frequency coaxial cables. The power relationship between the transmitter and receiver is shown in equation (12).

$$\begin{cases} \tilde{P}_{rx} = \tilde{P}_{tx} - L_{sys} - L_{atte} \\ P_{rx} = P_{tx} - L_{sys} - L_{path} + G_{tx} + G_{rx} \end{cases} \tag{12}$$

In equation (12), $\tilde{P}_{rx}$ denotes the received power during calibration, $\tilde{P}_{tx}$ denotes the set power of the transmitter during calibration, $L_{sys}$ denotes other losses except the path loss, $L_{atte}$ denotes the value of the attenuator, $P_{rx}$ denotes the received power during measurement, $P_{tx}$ denotes the set power of the transmitter during measurement, $L_{path}$ denotes the path loss, $G_{tx}$ denotes the gain of the transmitter, and $G_{rx}$ denotes the gain of the receiver. The actual path loss can be obtained from equation (12), and its calculation equation is shown in equation (13).

$$L_{path} = P_{tx} - P_{rx} + \tilde{P}_{rx} - \tilde{P}_{tx} + G_{tx} + G_{rx} + L_{atte} \tag{13}$$

In equation (13), the attenuator value is 60 dB. While in large scale modelling, the path loss model is shown in equation (14).

$$\begin{cases} PL_{LOS} = 31.48 + 21.50\log_{10}(d_{3D}) \\ \qquad + 19.00\log_{10}(f_c) + \chi_\sigma \\ PL_{NLOS} = \max(PL, PL_{LOS}) \\ PL = 32.4 + 23.0\log_{10}(d_{3D}) \\ \qquad + 20\log_{10}(f_c) + \chi_\sigma \end{cases} \tag{14}$$

In equation (14), $PL_{LOS}$ denotes the path loss model in the line-of-sight scenario, $d_{3D}$ denotes the spatial distance between the transmitting antenna and the receiving antenna, $f_c$ denotes the relative carrier frequency, $\sigma$ denotes the shadow fading factor, $PL$ denotes the conventional path loss model, and $PL_{NLOS}$ denotes the path loss in the non-line-of-sight scenario. Meanwhile, in actual measurements, it is necessary to test the overall linear interval of the system due to different linear intervals between modules. This calculation requires determining the theoretical value of the receiver's sensitivity, as shown in equation (15).

$$\begin{aligned} RX_{sens} &= -147dBm / Hz + 10 * \log_{10}(le9)Hz \\ &= -57dBm \end{aligned} \tag{15}$$

In equation (15), $RX_{sens}$ denotes the sensitivity at standard temperature. It is found that the noise power will be distorted when the input power is less than −57 dBm.

## 3. Result and Discussion

The study analyses the CM approach in a 5G communication environment, analyses the collected data on small and large scales, and compares it with the 3GPP channel model to confirm its accuracy. The transmitting and receiving antennas' heights are 3430 mm and 1590 mm, respectively, and their respective gains are 3 dBi and 22 dBi in this experiment. The transmitting end's power is adjusted at 43 dBm. The type of the transmitting antenna is omnidirectional, and the polarization direction is vertical; the type of the receiving antenna is PAA of 8*8 and the polarization direction is horizontal. The scanning range of the horizontal plate and the vertical beam are (–45°, 45°), and the scanning step and the number of beams are 5° and 361, respectively. The measurement bandwidth is 1 GHz and the number of samples and the frequency at the receiving end are 16384 and 6.4 Gsample/s, respectively. The measurable maximum time delay is 25.6 μs. Figure 7 displays the fitted curves of the measured route loss in both the non-line-of-sight scenario and line-of-sight scenario.

In the line-of-sight scenario shown in Figure 7(a), the measured route loss is less than the free-space loss model. When the distance is 1 m, the path loss is 61 dBm for both the free-space loss model and the CI fit, and 54 dBm and 59 dBm for the AB fit and the 3GPP model, respectively. The measured route loss in the non-line-of-sight scenario shown in Figure 7(b) is greater than the free-space loss model. When the distance is 1 m, the path loss is 69 dBm for the AB fit and 61 dBm for the free-space loss model, the CI fit, and the 3GPP model. Overall, it seems that the AB model is a better fit. The difference between the CI and AB models is due to the larger shadow fading factor in the CI model, resulting in greater fluctuation of the shadow fading term. The path loss index of the CI model is slightly lower than that of the free space loss in the case of LOS, and slightly higher than 2 in the case of NLOS. The cumulative distribution probability of the shadow fading term in the line-of-sight scenario is shown in Figure 8.

According to Figure 8(a), the cumulative probability distribution of the CI model's shadow fading term essentially follows a normal distribution; at 5 dB, the probability distribution of the shadow fading term tends to be 1. When the shadow fading term is 5 dB, its probability distribution tends to be close to 1. The AB model's shadow fading term's cumulative probability distribution in Figure 8(b) likewise follows a normal distribution. When the shadow fading term is 4 dB, its probability distribution tends to be close to 1. Meanwhile, a K-S test is run to confirm the accuracy of the test results. The test results show that the Boolean variables are all 1 and the numerical variables are all greater than $\alpha$ ($\alpha$ is the significant level with a preset value of 0.05). It is found that the cumulative probability distributions of the shadow fading terms of both the CI model and the AB model obey the normal distribution under the line-of-sight scenario. Figure 9 displays the shadow decay term's cumulative probability distribution for the non-line-of-sight distance scenario.

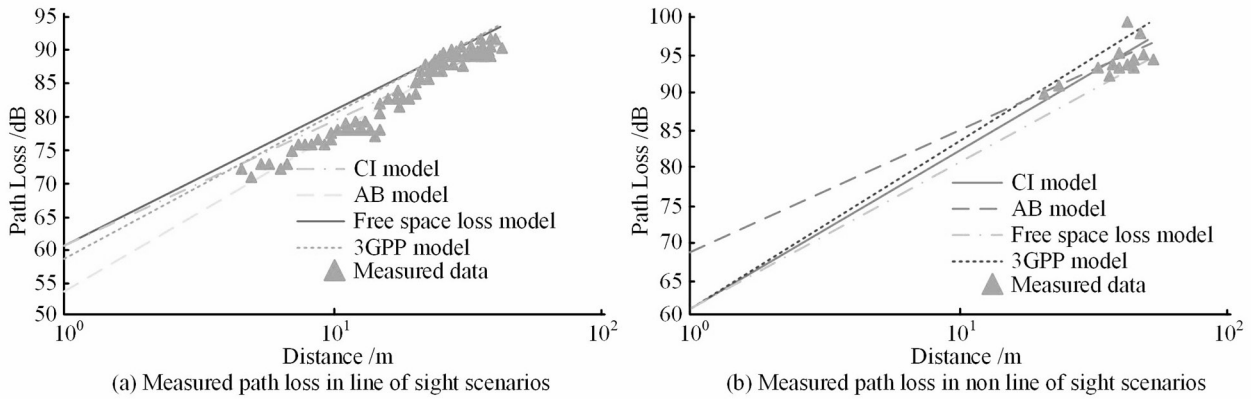


*Figure 7.* Measured path loss fitting curve in the line-of-sight scenario and non-line-of-sight scenario.

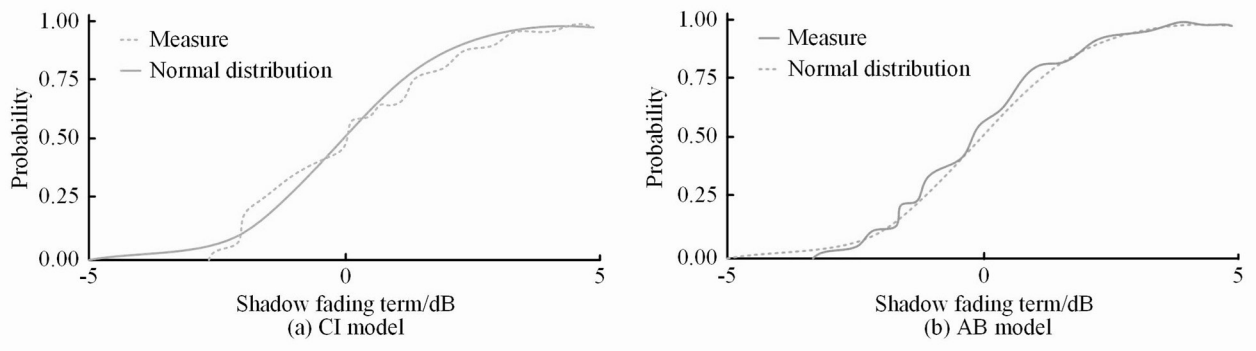


*Figure 8.* Cumulative probability distribution of shadow fading terms in distance-of-view scenarios.

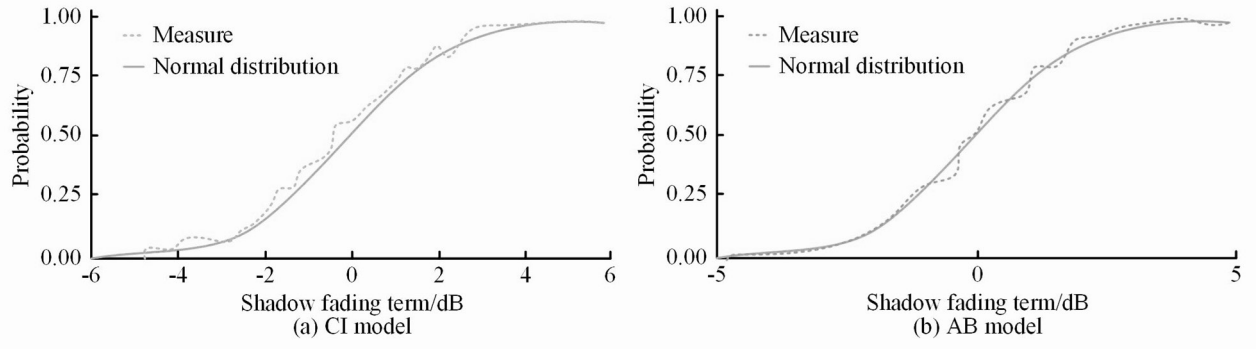


*Figure 9.* The cumulative probability distribution of shaded fading terms in non-line-of-sight scenario.

According to Figure 9(a), in the non-line-of-sight scenario, the cumulative probability distribution of the CI model's shadow fading term essentially follows a normal distribution. When the shadow fading term is 4 dB, its probability distribution tends to be close to 1. Figure 9(b) shows that the shadow fading term in the AB model follows a normal distribution in its cumulative probability distribution. The probability distribution reaches 1 at a shadow fading term of 3 dB. To confirm the precision of this finding, a K-S test was conducted. The test results show that the Boolean variables of both are 0 and the numerical variables are greater than $\alpha$. It is found that the cumulative probability distributions of the shadowing decay terms of the CI model and the AB model in the non-line-of-sight scenario do obey a normal distribution. The power time delay spectra for line-of-sight scenario and non-line-of-sight scenario are shown in Figure 10.

In Figure 10, the received power in both line-of-sight scenario and non-line-of-sight scenario basically rises and then falls with the increase of the time delay. When the time delay is 115 ns, the received power in both line-of-sight scenario and non-line-of-sight scenario reaches the maximum, and its received power is −97 dBm and −99 dBm, respectively, and the measured dynamic range of both of them is greater than 40 dBm. The extended logarithmic mean distributions of the time delay in LSS and non-line-of-sight scenario are shown in Figure 11.

The root-mean-square delay extensions' median and mean values are 38.6 ns and 39.9 ns, respectively. The log-mean distribution of the actual measured delay extensions in the line-of-sight scenario is shown in Figure 11(a) as a good fit to the 3GPP model, with log-mean and its standard deviation of −7.4 and 0.12, as opposed to log-mean and the standard deviation of −7.4 and 0.15, respectively, for 3GPP. Figure 11(b) shows that the log-mean distribution of actual measured delay extensions in the non-line-of-sight scenario is less compatible with the 3GPP model. The median and mean val-

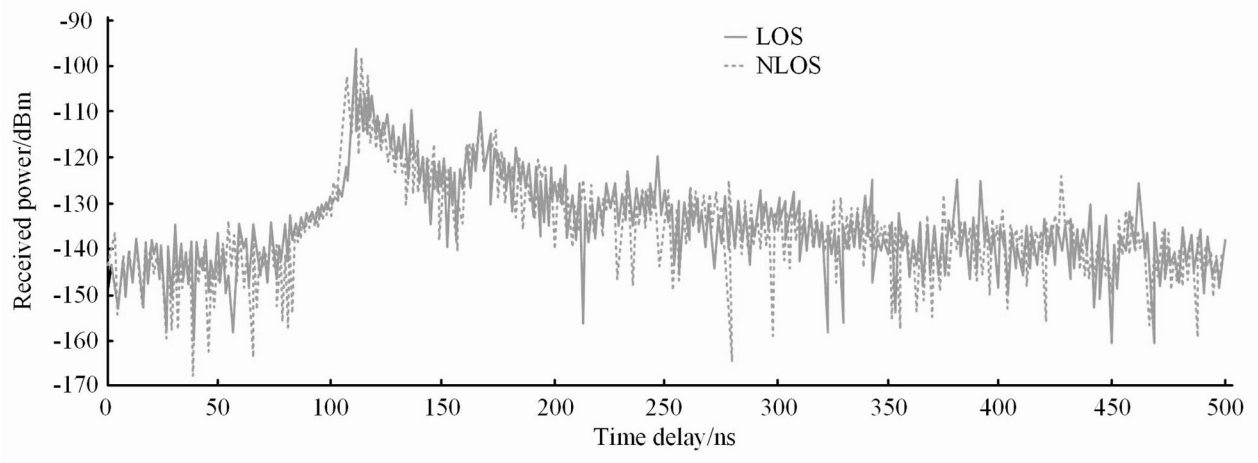


*Figure 10.* Power time delay spectrum.

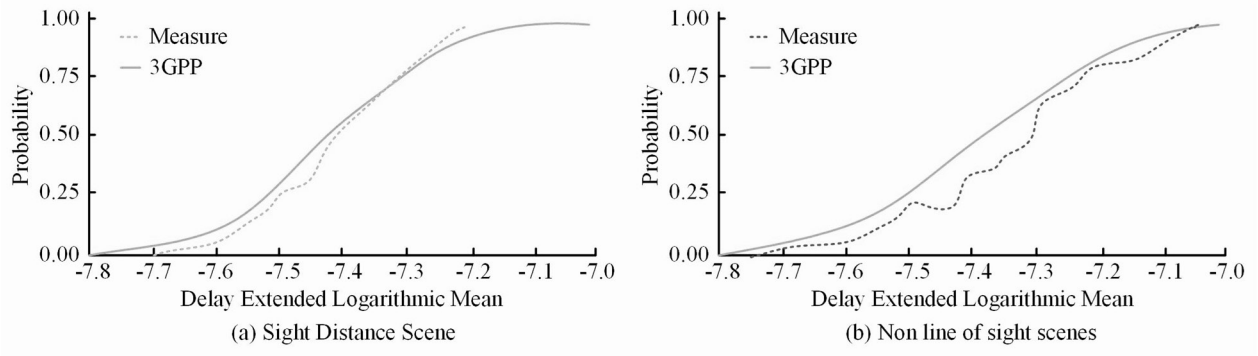


*Figure 11.* Time-delay-extended log-mean distribution.

ues of the root-mean-square delay extensions are 48.8 ns and 49.7 ns, respectively. Furthermore, the log-mean and its standard deviation values are −7.3 and 0.17, respectively, which differ slightly from the 3GPP's values of −7.4 and 0.19. The above results show that the actual measured delay extended log-mean and standard deviation are very close to the 3GPP model, which shows that the CM method proposed in the study can effectively achieve the measurement of delay domain parameters. The angular extended probability distribution and its mean and standard deviation are shown in Figure 12.

In Figure 12(a), the enlarged ranges for pitch angle of arrival and azimuth angle of arrival in the line-of-sight scenario are 14° to 31° and 14° to 29°, respectively, and 21° to 33° and 19° to 37°, respectively, for the non-line-of-sight scenario. From Figure 12(b), the log mean (LM) and standard deviation (SD) of the extended pitch angle of arrival for the 3GPP model in the line-of-sight scenario are 1.21 and 0.35, and those of the azimuth angle of arrival are 1.53 and 0.37, respectively. The LM and SD of the extended pitch angle of arrival for the actual measured data are 1.32 and 0.09, respectively. The LM and SD of the azimuth angle of arrival were 1.35 and 0.08, respectively. The LM of the pitch angle of arrival of the actual measured data is higher than that of the 3GPP model, while the LM of the azimuth angle of arrival is smaller than that of the 3GPP model. The non-line-of-sight scenario and LSS share the same relationship between the angular extension LM and SD of the actual observed data and the 3GPP model. The reason for these results is that the 3GPP model lacks the correlation between the density of structural bodies and spatial properties.

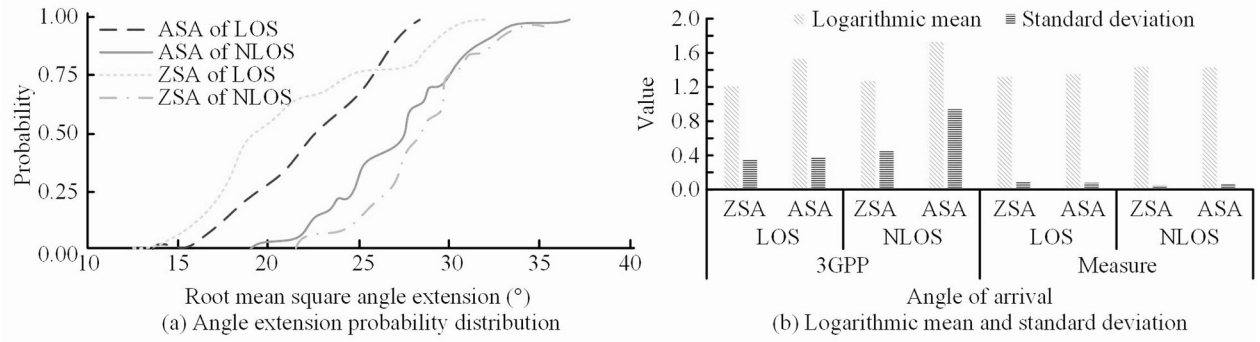


*Figure 12.* Angle extension probability distribution and its mean, standard deviation.

## 4. Conclusion

MW is a fundamental technology for 5G applications, offering numerous advantages, including large bandwidth, low null delay, and flexible, elastic null configuration. However, in the context of 5G-MW, the characteristics of its large bandwidth can result in high accuracy requirements and complex parameter analysis, leading to several challenges. To tackle these challenges and achieve precise measurements of 5G-MW channels, this study proposes a PAA-based CM method, which has been successfully tested. The experiment's findings show that the AB model and the measured path loss consequences agreed the best. However, there was less of a fit with the 3GPP model, CI model, and free space loss model. The cumulative probability distributions of the shadow fading term in the actual measured data follow a normal distribution in both line-of-sight scenario and non-line-of-sight scenario. Furthermore, all the Boolean variables showed a value of 1 and the numerical variables were greater than $\alpha$, as confirmed by the K-S test. It is worth highlighting that technical terms will be explained upon their first usage. The obtained results demonstrate accuracy and reliability. The received power increases and then decreases with increasing delay in various scenarios. Notably, the received power reaches its peak when the delay is 115 ns for both line-of-sight scenario and non-line-of-sight scenario. The recorded received power values are –97 dBm and –99 dBm correspondingly, with dynamic ranges more than 40 dBm. The delays for the LSS and non-line-of-sight scenario are –7.4 and –7.3, respectively, with SDs of 0.15 and 0.17. All the data are in close proximity to the 3GPP model. The results indicate that the parameters of the CM method proposed in the study align with those of the standard model, and the differences are acceptable. Therefore, it is evident that the suggested method can accurately quantify the 5G-MW channel. The research method employs phased array technology, which enables rapid measurement of angular information throughout space by scanning the beam quickly. This ensures antenna gain and maintains a large dynamic range of measurement. The method is applicable to CM and parameter extraction, providing a valuable reference for research on 5G industrial Internet of Things. While the proposed approach is deemed more dependable, the significant bandwidth aspect of 5G-MW leads to limited computational resources on the digitizer. Consequently, forthcoming studies will concentrate on enhancing the real-time analysis and Doppler measurement proficiency of the system.

## References

[1] L. Kou *et al.*, "Simulation and Sensitivity Analysis for Cloud and Precipitation Measurements Via Spaceborne Millimeter-wave Radar", *Atmospheric Measurement Techniques*, vol. 16, no. 6, pp. 1723–1744, 2023. http://dx.doi.org/10.5194/amt-16-1723-2023

[2] J. Tang *et al.*, "Physical Layer Authentication for 5G/6G Millimeter Wave Communications by Using Channel Sparsity", *IET Communications*, vol. 16, no. 3, pp. 206–217, 2022. http://dx.doi.org/10.1049/cmu2.12330

[3] S. Jiang *et al.*, "LiDAR Aided Future Beam Prediction in Real-World Millimeter Wave V2I Communications", *IEEE Wireless Communications Letters*, vol. 12, no. 2, pp. 212–216, 2023. http://dx.doi.org/10.1109/LWC.2022.3219409

[4] Y. T. Liao *et al.*, "Millimeter-wave Passive Patch Antenna for Use in Wireless High-temperature Sensor", *Sensors and Materials: An International Journal on Sensor Technology*, vol. 34, no. 6, pp. 2281–2292, 2022. http://dx.doi.org/10.18494/SAM3841

[5] Z. Zhang *et al.*, "Omnidirectional Oversized Annular Lens Antenna with High Gain for 5G Millimeter Wave Channel Measurement", *Microwave and Optical Technology Letters*, vol. 63, no. 10, pp. 2621–2627, 2021. http://dx.doi.org/10.1002/mop.32947

[6] I. Jericho and R. Jayadi, "An Empirical Study on the Factors Affecting Intention to Use 5G Technology", *Journal of System and Management Sciences*, vol. 13, no. 2, pp. 301–315, 2023. http://dx.doi.org/10.33168/JSMS.2023.0221

[7] T. Jiang *et al.*, "A Study of Uplink and Downlink Channel Spatial Characteristics in an Urban Micro Scenario at 28 GHz", *Frontiers of Information Technology & Electronic Engineering*, vol. 22, no. 4, pp. 488–502, 2021. http://dx.doi.org/10.1631/FITEE.2000443

[8] H. Mi *et al.*, "Multi-scenario Millimeter Wave Wireless Channel Measurements and Sparsity Analysis", *China Communications*, vol. 19, no. 11, pp. 16–31, 2022. http://dx.doi.org/10.23919/JCC.2022.11.002

[9] Q. Zhu *et al.*, "A General Altitude-dependent Path Loss Model for UAV-to-ground Millimeter-wave Communications", *Frontiers of Information Technology & Electronic Engineering*, vol. 22, no. 6, pp. 767–776, 2021. http://dx.doi.org/10.1631/FITEE.2000497

[10] S. H. Lim *et al.*, "Deep Learning-based Beam Tracking for Millimeter-wave Communications under Mobility", *IEEE Transactions on Communications*, vol. 69, no. 11, pp. 7458–7469, 2021. http://dx.doi.org/10.1109/TCOMM.2021.3107526

[11] M. Cho, "ETE Model and High Precision Positioning for Autonomous Flight in 5G", *Journal of System and Management Sciences*, vol. 12, no. 2, pp. 315–324, 2022. http://dx.doi.org/10.33168/JSMS.2022.0215

[12] R. Xiao *et al.*, "A W-band Sparse PhasedArray Antenna with Ultrahigh Sparsity for Radar Applications", *Microwave and Optical Technology Letters*, vol. 64, no. 3, pp. 525–529, 2021. http://dx.doi.org/10.1002/mop.33111

[13] T. Hirasawa *et al.*, "Fabrication and Evaluation of Integrated Photonic Array-Antenna System for RoF Based Remote Antenna Beam Forming", *IEICE Transactions on Electronics*, vol. 102, no. 3, pp. 235–242, 2019. http://dx.doi.org/10.1587/transele.2018ECP5043

[14] Z. Zhou *et al.*, "A High-precision and Fast Off-line Beamforming Pattern Estimation Technique for Active Phased Array Antenna Application", *International Journal of RF and Microwave Computer-Aided Engineering*, vol. 32, no. 8, pp. 23247–23253, 2022. http://dx.doi.org/10.1002/mmce.23247

[15] M. K. Cho and Y. H. Chun, "High-Precision Position Protocol for Vehicle to Pedestrian using 5G Networks", *Journal of System and Management Sciences*, vol. 12, no. 1, pp. 241–253, 2022. http://dx.doi.org/10.14704/web/v19i1/web19309

[16] E. S. Parshina, "Technique for Spatial Interference Reduction and Its Application in Monopulse Radar with Active Phased Array Antenna", *Issues of Radio Electronics*, no. 12, pp. 17–22, 2021. http://dx.doi.org/10.21778/2218-5453-2020-12-17-22

[17] W. Li *et al.*, "The Test of Phased Array Antenna for Marine Seismic Data Transmission", *Procedia Computer Science*, vol. 183, no. 5, pp. 372–378, 2021. http://dx.doi.org/10.1016/J.PROCS.2021.02.073

[18] M. A. Oyegoke and Y. O. Olasoji, "PAPR Reduction in OFDM Systems Using Hybrid Zadoff-Chu Transform Precoding and Partial Transmit Sequence", *European Open Science Publishing*, vol. 33, no. 5, pp. 1619–1629, 2021. http://dx.doi.org/10.24018/ejece.2021.5.5.362

[19] S. Abdallah *et al.*, "Joint Timing-offset and Channel Estimation for Physical Layer Network Coding in Frequency Selective Environments", *IET Communications*, vol. 15, no. 15, pp. 1917–1929, 2021. http://dx.doi.org/10.1049/cmu2.12203

[20] I. Jericho and R. Jayadi, "An Empirical Study on the Factors Affecting Intention to Use 5G Technology", *Journal of System and Management Sciences*, vol. 13, no. 2, pp. 301–315, 2023. http://dx.doi.org/10.33168/JSMS.2023.0221

[21] G. Paryanti and D. Sadot, "Real-Valued Neural Networks for Complex-Valued Impairment Compensation Using Digital Up-Conversion", *IEEE Transactions on Communications*, vol. 68, no. 12, pp. 7511–7520, 2020. http://dx.doi.org/10.1109/TCOMM.2020.3025363

[22] T. Liu *et al.*, "Parallel Wideband Digital Up-conversion Architecture With Efficiency", *The Journal of Engineering*, vol. 2019, no. 23, pp. 8587–8590, 2019. http://dx.doi.org/10.1049/joe.2018.9061

[23] Z. Feng *et al.*, "Low Power Structure Digital Up Converter Design for Software Radio System", *Journal of Circuits, Systems and Computers*, vol. 20, no. 2, pp. 1–11, 2020. http://dx.doi.org/10.1142/S0218126621500195

[24] Z. Chen, "Research on Internet Security Situation Awareness Prediction Technology Based on Improved RBF Neural Network Algorithm", *Journal of Computational and Cognitive Engineering*, vol. 1, no. 3, pp. 103–108, 2022. http://dx.doi.org/10.47852/bonviewJCCE149145205514

[25] Y. Fang *et al.*, "ST-SIGMA: Aggregation of Spatiotemporal Semantics and Interaction Graphs for Multi-agent Perception and Trajectory Prediction", *CAAI Intelligence Technology Transactions*, vol. 7, no. 4, pp. 744–757, 2022. http://dx.doi.org/10.1049/cit2.12145

*Received:* October 2023
*Revised:* January 2024
*Accepted:* January 2024

*Contact address*:
Yu Qian
School of Rail Transportation
Southwest Jiaotong University Hope College
Chengdu
Sichuan
China
e-mail: yq103123@126.com

Yu Qian received the ME degree from Chengdu University of Technology in 2018. Now, she works as an assistant director at Southwest Jiaotong University Hope College. Her research interests include computational intelligence, wireless communication, and big data analysis.